CHIN. PHYS. LETT. Vol. 37, No. 8 (2020) 087105 **Express Letter**

Symmetry-Assisted Protection and Compensation of Hidden Spin Polarization in Centrosymmetric Systems

Yingjie Zhang(张英杰)[1†], Pengfei Liu(刘鹏飞)[1†], Hongyi Sun(孙红义)[1†], Shixuan Zhao(赵世轩)[1], Hu Xu(徐虎)[1], and Qihang Liu(刘奇航)[1,2,3*]

[1]*Shenzhen Institute for Quantum Science and Technology and Department of Physics, Southern University of Science and Technology, Shenzhen 518055, China*
[2]*Guangdong Provincial Key Laboratory for Computational Science and Material Design, Southern University of Science and Technology, Shenzhen 518055, China*
[3]*Center for Quantum Computing, Peng Cheng Laboratory, Shenzhen 518055, China*

(Received 23 June 2020; accepted 14 July 2020; published online 21 July 2020)

It was recently noted that in certain nonmagnetic centrosymmetric compounds, spin–orbit interactions couple each local sector that lacks inversion symmetry, leading to visible spin polarization effects in the real space, dubbed "hidden spin polarization (HSP)". However, observable spin polarization of a given local sector suffers interference from its inversion partner, impeding material realization and potential applications of HSP. Starting from a single-orbital tight-binding model, we propose a nontrivial way to obtain strong sector-projected spin texture through the vanishing hybridization between inversion partners protected by nonsymmorphic symmetry. The HSP effect is generally compensated by inversion partners near the Γ point but immune from the hopping effect around the boundary of the Brillouin zone. We further summarize 17 layer groups that support such symmetry-assisted HSP and identify hundreds of quasi-2D materials from the existing databases by first-principle calculations, among which a group of rare-earth compounds LnIO (Ln = Pr, Nd, Ho, Tm, and Lu) serves as great candidates showing strong Rashba- and Dresselhaus-type HSP. Our findings expand the material pool for potential spintronic applications and shed light on controlling HSP properties for emergent quantum phenomena.

PACS: 71.70.Ej, 85.75.−d, 61.50.Ah DOI: 10.1088/0256-307X/37/8/087105

Spin polarization, generally measured by the difference between spin-up and spin-down electrons for a given direction $S = (I_\uparrow - I_\downarrow)/(I_\uparrow + I_\downarrow)$, was thought to be limited to magnetic materials such as Fe or Ni. The current paradigm, however, shows that spin polarization is possible also in nonmagnetic crystals with strong spin-orbit coupling (SOC) and broken inversion symmetry.[1] Recently, it was shown that in certain centrosymmetric crystals where the energy bands are at least two-fold degenerate, the inversion-asymmetric sectors also manifest Rashba- or Dresselhaus-type spin textures.[2] For a local sector (named A), such as a monolayer of 2H-MoS_2[3,4] and a BiS_2 sublayer of $LaOBiS_2$,[5,6] such a form of "hidden spin polarization" (HSP) is calculated by projecting the Bloch wavefunctions $\psi_n(\boldsymbol{k})$ of the doubly degenerate bands on sector A, which can be written as follows:

$$\boldsymbol{S}^{\mathrm{A}}_{\mathbb{N}}(\boldsymbol{k}) = \sum_{i\in A}\sum_{n\in\mathbb{N}}\langle\psi_n(\boldsymbol{k})|(\boldsymbol{\sigma}\otimes|i\rangle\langle i|)|\psi_n(\boldsymbol{k})\rangle, \quad (1)$$

where $\boldsymbol{k}$, $\boldsymbol{\sigma}$, and $|i\rangle$ denote the wavevector, Pauli operator, and the localized orbitals belonging to sector A. The band index $\mathbb{N}$ implies a summation over the two bands with degenerate energy. As an observable, $\boldsymbol{S}^{\mathrm{A(B)}}_{\mathbb{N}}(\boldsymbol{k})$ is independent of the choice of any unitary basis transformations of the two-dimensional (2D) wavefunction space, holding the potential for detectability. While HSP is an intrinsic property widely existing in crystals with inversion-asymmetric sectors, the word "hidden" implies that in general HSP cannot be directly measured without inversion symmetry breaking, but can be detected by local-probe techniques that distinguish different sectors. By using spin- and angle-resolved photoemission spectroscopy (ARPES) measurements, the HSP effect has been experimentally confirmed in a number of centrosymmetric bulk materials.[7−10] Very recently, HSP has been reported in traditional cuprates and thus prompts the open question of how high-temperature superconductivity correlates with such a nontrivial spin pattern.[11]

The discovery of HSP considerably broadens the range of materials for potential spintronic applications and brings exotic physical insights into the existing fields, such as spin field effect transistors,[5] spin switching of antiferromagnets,[12] topological insulators[13] and topological superconductivity.[14] Furthermore, the concept of HSP has triggered a broader field of "hidden polarization", where various physical effects have been recognized to be determined by the local symmetry breaking of a system, albeit with a higher global symmetry that seemingly prohibits the effect from happening. Examples include orbital polarization,[15] optical activity,[16] circular polarization,[3,17] Berry curvature,[18] Ising superconductivity,[19,20] etc.

This work was supported by the National Natural Science Foundation of China (Grant No. 11874195), the Guangdong Provincial Key Laboratory of Computational Science and Material Design (Grant No. 2019B030301001), and the Center for Computational Science and Engineering of SUSTech.
†These authors contributed equally to this work.
*Corresponding author. Email: liuqh@sustech.edu.cn
© 2020 Chinese Physical Society and IOP Publishing Ltd

Based on the symmetry analysis of the atomic sites or sectors,[2] most centrosymmetric materials would be expected to manifest HSP, especially for quasi-2D layered materials with finite thickness. However, materials with strong HSP that hold realistic potential for applications indeed form a much smaller subgroup. For example, silicon, germanium and tin in diamond structure are nominal Dresselhaus-type HSP systems because each X (X = Si, Ge, or Sn) atom has an inversion-asymmetric $T_{\rm d}$ site point group, leading to opposite Dresselhaus spin textures localized at the two X sublattices. However, the strong coupling between the two X sublattices (hopping term through the X–X bond) usually leads to strong hybridization between the two sublattices and thus significantly compensates for the HSP localized on each X atom. Therefore, after completing "proof of existence" for HSP, the next important question is which specific physical features within centrosymmetric crystals actually control the magnitude of such HSP effect, i.e., "where to look".[21] In addition to strong SOC that favors heavier elements, the design principle of HSP also requires to minimize the hybridization between sectors. One obvious but trivial way is to separate the two sectors as far as possible. This is analogous to the thick slab of a topological insulator with inversion symmetry, in which the top and bottom surfaces manifest energy-degenerate Dirac cones and spin polarizations with opposite chirality.[22] Such a type of HSP is fundamentally two individual sets of spin polarization in quite different places, which is difficult to manipulate and integrate in one system.

Here, we explore a nontrivial, symmetry-assisted approach to minimize the hopping effect between the inversion-asymmetric sectors and thus protect the HSP in each sector. Our tight-binding model reveals that when the two sectors connect with each other by nonsymmorphic crystalline symmetry, the electron hopping between sectors vanishes along the Brillouin zone (BZ) boundary and is strongly suppressed in the vicinity of the time-reversal invariant (TRI) momenta. As a result, a spin map constructed throughout the full BZ shows that nearly perfect HSP survives even though the two sectors are close to each other in a quasi-2D lattice. We further perform symmetry analysis and identify 17 quasi-2D layer groups (out of 80) in total that support such symmetry protected HSP. Among the realistic materials in the existing quasi-2D material databases[23,24] with the selected layer groups, we perform first-principle calculations and choose a rare-earth family LnIO (Ln = Pr, Nd, Ho, Tm, and Lu) as representative candidates showing strong Rashba and Dresselhaus HSP, which is in excellent agreement with our tight-binding model. Our finding offers a general principle for extensively exploring strong HSP materials and provides an ideal platform to control HSP for emergent physical properties. One possible example is to tune the hybridization gap of such an HSP system by tensile strain to realize time-reversal-invariant topological superconductivity.[14,25,26]

HSP from a Single-Orbital Tight-Binding Model. We begin with a simple model of a nonsymmorphic 2D lattice to illustrate how HSP in one sector survives under the existence of its inversion partner. Considering a square lattice with only two identical atoms (A and B) in a unit cell with a small displacement between them along the z direction [see Fig. 1(a)], such a buckling structure has a $p4/nmm$ layer group with glide mirror reflection $\{M_z|(1/2,1/2,0)\}$ and screw axis operations $\{C_{2x}|(1/2,0,0)\}$ and $\{C_{2y}|(0,1/2,0)\}$. In addition, the buckling also creates opposite local polar fields felt by each sector (here, each atom forms a sector) along the $\pm z$ direction, rendering a Rashba-type HSP system. Therefore, we can easily construct the single-orbital (e.g., s, p_z or d_{z^2}) tight-binding model (four bands) as follows:

$$H(\boldsymbol{k}) = t_1 \cos\frac{k_x}{2}\cos\frac{k_y}{2}\tau_x\sigma_0 + t_2(\cos k_x + \cos k_y)\tau_0\sigma_0 + \lambda_{\rm R}(\sin k_x\sigma_y - \sin k_y\sigma_x)\tau_z, \quad (2)$$

where τ and σ are Pauli matrices describing the sector and spin degrees of freedom, respectively. The derivation of Eq. (2) is provided in Section A of Supplementary Material. The first (second) term describes the nearest (next nearest) neighbor hopping, while the third term presents Rashba SOC caused by local polar fields. The band structures of Eq. (2) is shown in Fig. 1(b). In the absence of SOC ($\lambda_{\rm R} = 0$), only the second term of Eq. (2) survives along the BZ boundary, leading to double degeneracy (excluding spin), i.e., the "band sticking" effect due to nonsymmorphic symmetry.[27] When including SOC, the energy bands along the BZ boundary generally split into two doubly degenerate bands, except at the high-symmetry TRI momenta X and M. This is because at these points, a nonsymmorphic symmetry fulfills the anticommutation relationship with the inversion operator, leading to an extra two-fold degeneracy between two pairs of Kramers degeneracy, i.e., four-fold degeneracy.[28,29]

Nonsymmorphic symmetry has recently drawn extensive attention due to such band degeneracy effects, leading to new types of quasiparticles, such as Dirac nodes,[29–32] nodal chains,[33] and nodal surfaces.[34] However, its impact on the spin textures as well as Bloch states of different sublattices has not yet been substantially explored.[35] To reveal this effect, we analytically solve Eq. (2) with the basis of $|A\uparrow\rangle$, $|A\downarrow\rangle$, $|B\uparrow\rangle$, $|B\downarrow\rangle$ (see Supplementary Section B). The resulting eigenstates are

$$\phi_1 = \frac{1}{\sqrt{2}}\begin{pmatrix}1\\ D_-/F\\ -M/F\\ 0\end{pmatrix},\ \phi_2 = \frac{1}{\sqrt{2}}\begin{pmatrix}0\\ -M/F\\ -D_+/F\\ 1\end{pmatrix},$$
$$\phi_3 = \frac{1}{\sqrt{2}}\begin{pmatrix}1\\ -D_-/F\\ M/F\\ 0\end{pmatrix},\ \phi_4 = \frac{1}{\sqrt{2}}\begin{pmatrix}0\\ M/F\\ D_+/F\\ 1\end{pmatrix}, \quad (3)$$

where $M = t_1\cos(k_x/2)\cos(k_y/2)$, $N = t_2(\cos k_x + \cos k_y)$, $D_+ = \lambda_{\rm R}(\sin k_y + i\sin k_x)$, $D_- = D_+^\dagger$, and

$F = \sqrt{M^2 + D_+ D_-}$. In order to quantify and minimize the mixture of wavefunctions between different sectors, we then define a quantity named sector polarization $P_n^{\rm sec}(\boldsymbol{k}) = (\rho_n^{\rm A} - \rho_n^{\rm B})/(\rho_n^{\rm A} + \rho_n^{\rm B})$, where $\rho_n^{\rm A/B} = \sum_{i\in {\rm A/B}} \langle \phi_n(\boldsymbol{k})|i\rangle\langle i|\phi_n(\boldsymbol{k})\rangle$ is the module squared wavefunction projected onto sector A or B. Note that in quantum mechanics, if two eigenstates are degenerate, any linear combination of the two states is also an eigenstate of the system. Therefore, $P_n^{\rm sec}$ is gauge variant for a single branch of doubly degenerate bands, depending on the unitary transformation of basis that mixes ϕ_1 and ϕ_2 (while HSP is gauge invariant, see below). When a certain form of inversion-symmetry breaking is introduced, such as a tiny electric field along the z direction, a definitive gauge (in this case $\{\phi_1, \phi_2\}$ and $\{\phi_3, \phi_4\}$) is picked up.

The sector polarization $P_n^{\rm sec}(\boldsymbol{k})$ of the lowest doubly degenerate bands and eigenstates $\{\phi_1, \phi_2\}$ are shown in Fig. 1(c). The most important feature is that at the BZ boundary X–M, $P_n^{\rm sec}$ is pinned to its maximum value ± 1, indicating a vanishing hopping effect between sectors A and B. In sharp contrast, the sector polarization at the Γ point is exactly zero. These observations can be explained by the model Hamiltonian, where the off-diagonal matrix elements are contributed solely by the first term of Eq. (2) containing τ_x. At the BZ boundary, the first term vanishes, and the Hamiltonian is the direct sum of two matrices separately exerted on two subspaces spanned by two sectors. Therefore, the two eigenstates are naturally chosen to be located in either sector A or B, leading to maximum sector polarization. This is analogous to the fact that two bands with different group representations do not hybridize when they meet each other, leading to a degenerate band-crossing point. In either case, the representation space of this special point can be spanned as a direct sum of two subspaces from the two crossing bands. On the other hand, when the wavevector moves to Γ from the BZ boundary, the τ_x term of Eq. (2) becomes more predominant, leading to descending $P_n^{\rm sec}$ with the electron density finally distributed equally in A and B sectors at Γ. Note that if we do not consider any symmetry requirements but just separate the two sectors very far away from each other, the τ_x term of Eq. (2) also vanishes because of the negligible hopping parameter t_1. However, such a strategy is just a trivial overlap of two individual inversion-asymmetric systems in k-space and is not useful for real material design.

The direct consequence of full sector polarization is that the HSP also reaches its maximum value at the BZ boundary. The sector-projected spin polarization is calculated by projecting the wavefunction on sector A or B, as written in Eq. (1). Remarkably, $\boldsymbol{S}_{\mathbb{N}}^{\rm A(B)}(\boldsymbol{k})$ is independent of the choice of unitary basis transformation, indicating an observable (see Section B of Supplementary Material). The sector-projected spin textures on sector A and B are shown in Fig. 1(d). At the BZ boundary, both inversion-asymmetric sectors retain large but opposite HSP. Such spin polarization signals can be measured by spin-ARPES when the local probe is located at sector A or B. In sharp contrast, around the Γ point, the HSP localized at one sector is almost fully compensated by its inversion partner because the corresponding wavefunction contains a substantial mixture of the two sublattices, leading to vanishing $P_n^{\rm sec}$. Interestingly, we note that around the TRI momenta, the projected spin textures are Rashba-type at the M point but Dresselhaus-type at the X point, validating that the symmetry requirement of the Rashba effect always suggests an accompanying Dresselhaus effect.[2] Specifically, the low energy effective $k\cdot p$ Hamiltonians expanded by the SOC term of Eq. (2) takes the form of $(k_x\sigma_y - k_y\sigma_x)\tau_z$ at M, while $(k_x\sigma_y + k_y\sigma_x)\tau_z$ at X, indicating Rashba- and Dresselhaus-type spin patterns, respectively.

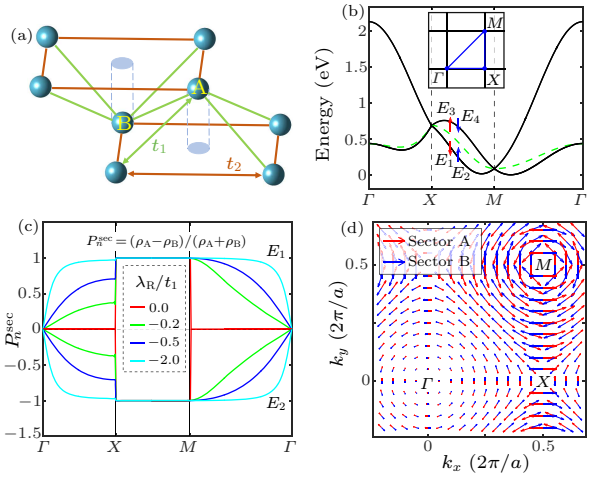

Fig. 1. (a) A square lattice with two identical atoms (A and B) in one unit cell. The nonsymmorphic symmetry is caused by the atomic displacement along the z direction. t_1 (t_2) is the nearest (next nearest) neighbor hopping parameter. (b) Band structure of this square lattice without and with SOC ($\lambda_{\rm R}/t_1 = -0.2$). (c) Sector polarization ($P_n^{\rm sec}$) of the lowest two doubly-degenerate bands E_1 and E_2 for different strength of Rashba SOC $\lambda_{\rm R}$ induced by the local polar field. (d) Projected spin texture onto sector A (red) and B (blue) for the lowest two bands E_1 and E_2 ($\lambda_{\rm R}/t_1 = -0.2$).

The sector polarization for different SOC strengths (quantified by $\lambda_{\rm R}/t_1$) is also shown in Fig. 1(c). The main variation lies in the descending trends from M and X to Γ. Along these directions, the sector polarization $P_n^{\rm sec}$ increases with $\lambda_{\rm R}/t_1$, indicating that in Eq. (2) the SOC term containing τ_z enhances the polarization, while the intersector coupling term containing τ_x suppresses the polarization. The results shown in Fig. 1(c) clearly indicate that in certain nominal HSP materials, such as silicon, the magnitude of HSP would be very small because of the large hopping parameter between two silicon atoms and the small SOC strength. Consequently, it is desirable to have the protected HSP effect forming a large domain throughout the BZ by tuning the SOC strength relative to the intersector coupling.

Symmetry Consideration and Other Prototypical Nonsymmorphic Structures. For the realization of realistic materials that manifest strong Rashba HSP, we

next construct some symmetry requirements as design principles and scan the stable quasi-2D material databases, including Materialsweb[23] and AiiDA,[24] to select ideal candidates with our target property. The reason we choose such layered materials is to build a straightforward connection with our tight-binding model. Since Rashba HSP requires a principle axis that is favored by layered structures, our screening process can be easily generalized to 3D Rashba hidden spin systems (such as $LaOBiS_2$[2] and $BaNiS_2$[36,37]). We choose layer groups (80 in total) to classify the symmetry of quasi-2D materials, which greatly narrows the range of 3D space groups (230 in total) that need to be considered. The correspondence between all the layer groups and space groups is provided in the process of classification, as shown in Section C of Supplementary Material.

Table 1. List of layer groups with inversion symmetry and nonsymmorphic symmetry and the corresponding quasi-2D materials.

Point group	Layer group	Space group	# of materials	Representative materials
C_{2h}	L15 $p2_1/m11$	11 $P2_1/m$	49	AgBr
	L16 $p2/b11$	13 $P2/c$	8	Pr_2I_5
	L17 $p2_1/b11$	14 $P2_1/c$	31	AgF_2
D_{2h}	L38 *pmaa*	49 *Pccm*	0	-
	L39 *pban*	50 *Pban*	1	$BaP_2(HO)_4$
	L40 *pmam** L41 *pmma**	51 *Pmma*	10	CuHgSeBr
	L42 *pman*	53 *Pmna*	7	P
	L43 *pbaa*	54 *Pcca*	0	-
	L44 *pbam*	55 *Pbam*	2	WBr_2
	L45 *pbma*	57 *Pbcm*	1	SiO_2
	L46 *pmmn*	59 *Pmmn*	43	$ZrTe_5$
	L48 *cmme*	67 *Cmme*	3	TlF
C_{4h}	L52 $p4/n$	85 $P4/n$	4	$MoPO_5$
D_{4h}	L62 $p4/nbm$	125 $P4/nbm$	0	-
	L63 $p4/mbm$	127 $P4/mbm$	1	$MoBr_2$
	L64 $p4/nmm$	129 $P4/nmm$	64	LuIO

*Layer group *pmam* (L40) and *pmma* (L41) are distinguished from each other by the direction of the glide mirror, and these two layer groups correspond to the same 3D space group Pmma.

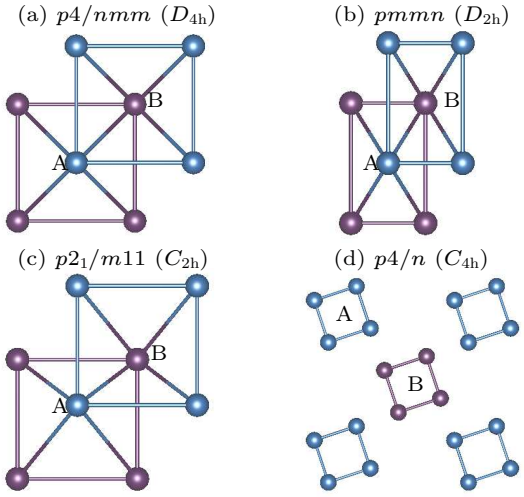

Fig. 2. Top view of the prototypical structures for (a) layer group $p4/nmm$ (D_{4h}, No. L64), (b) layer group $pmmn$ (D_{2h}, No. L46), (c) layer group $p2_1/m11$ (C_{2h}, No. L15) and (d) layer group $p4/n$ (C_{4h}, No. L52). Balls with different colors denote identical atoms but have different coordination along the z direction.

The initial symmetry conditions are inversion symmetry and nonsymmorphic symmetry, which have been shown to protect HSP at the BZ boundary in our model calculation. This search yields 17 layer groups from 4 point groups C_{2h}, D_{2h}, C_{4h} and D_{4h} and 225 material candidates from the chosen databases (see Table 1). For the C_{4h} point group, there is only one layer group $p4/n$, which requires at least eight atoms to construct. On the other hand, we note that $p2_1/m11$, $pmmn$, and $p4/nmm$ (belonging to C_{2h}, D_{2h}, and D_{4h}, respectively) are the three layer groups with the largest number of materials. They can be constructed by only two identical atoms, representing a total of 156 materials.

The prototypical structures of the four point groups are shown in Fig. 2. The model Hamiltonian of the structure for layer group $p4/nmm$ (D_{4h}) has been introduced in Eq. (2). The prototypical structure $p4/n$ (C_{4h}) is built by putting a set of general positions in the lattice because any simpler structures that include a set of special positions in the lattice turn out to be structures with space groups of higher symmetry such as $p4/nmm$. Then, by taking each of the four clustered atoms as a sector, we can still build a 4×4 effective Hamiltonian similar to Eq. (2).

Similarly, the prototypical structure for layer group $pmmn$ (D_{2h}) can be easily constructed by using the same analysis as Eq. (2), except using a rectangular lattice rather than a square lattice, in the following form:

$$\begin{aligned} H(\boldsymbol{k}) = {} & t_1 \cos\frac{k_x}{2}\cos\frac{k_y}{2}\tau_x\sigma_0 \\ & + (t_{21}\cos k_x + t_{22}\cos k_y)\tau_0\sigma_0 \\ & + \lambda_{\mathrm{R}}(\sin k_x\sigma_y - \sin k_y\sigma_x)\tau_z. \end{aligned} \tag{4}$$

Then, from Eqs. (A5) and (A9) in Section A of Supplementary Material, we can obtain the one-orbital Hamiltonian of the $p2_1/m11$ structure with C_{2h} symmetry in Fig. 2(c). By substituting the concrete values

of $\boldsymbol{d}_{jl}$ into this expression, we obtain

$$\begin{aligned} H = & t_1 \cos\left(\frac{k_x}{2}\right)\cos\left(\frac{k_y}{2}\right)\tau_x\sigma_0 \\ & + [t_{21}\cos k_x + t_{22}\cos k_y]\,\tau_0\sigma_0 \\ & + t_1'\sin\left(\frac{k_x}{2}\right)\cos\left(\frac{k_y}{2}\right)\tau_y\sigma_0 \\ & + \lambda_{\mathrm{R}}[\sigma_y \sin k_x - \sigma_x \sin k_y]\tau_z \\ & + \lambda_{\mathrm{R}}' \sin k_y \tau_z\sigma_z, \end{aligned} \tag{5}$$

where $t_1 = 3\,t_{11} - t_{12}$, $t_1' = t_{12} - t_{11}$, and $\lambda_{\mathrm{R}}'/\lambda_{\mathrm{R}} \sim d_z/b$, which can influence the relative ratio of the z component relative to the xy component of HSP, while the total HSP is determined by λ_{R}/t_1. Among the four prototypical structures, $p2_1/m11$ ($C_{2\mathrm{h}}$) has the lowest symmetry. Due to the absence of a screw axis along the x direction, the four-fold degeneracy at the X point lifts, and the HSP along M–X is not enforced to its maximum value, as shown in Fig. 3(a). Interestingly, the spin polarization now has sizable s_z components peaked along M–X, in contrast to the other three representative layer groups in which the spin orientation is totally in-plane. This is because the reduced symmetry of $p2_1/m11$ leads to an additional term $\sin k_y \sigma_z \tau_z$ in the model Hamiltonian, as shown in Eq. (5). Thus, as shown in Fig. 3(b), the total HSP around M is still significant but experiences a visible out-of-plane canting from the $k_x - k_y$ plane (37° for the tight-binding parameters in Fig. 3).

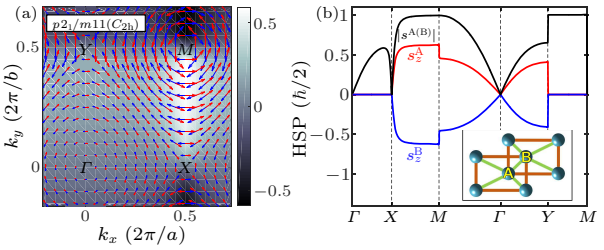

Fig. 3. (a) Projected spin texture onto sectors A (red) and B (blue) for the lowest two bands ($\lambda_{\mathrm{R}}/t_1 = -0.5$) of the $p2_1/m11$ structure ($C_{2\mathrm{h}}$). (b) Total HSP and the s_z component of the two sectors. The crystal structure is shown in the inset of panel (b).

Materials Realization. We next apply density functional theory (DFT) calculations, with the presence of SOC, to the material candidates selected by the symmetry principles described above. Our first-principle calculations use the projector-augmented wave (PAW) pseudopotentials[38] with the exchange-correlation of Perdew-Burke-Ernzerhof (PBE) form[39] as implemented in the Vienna *ab initio* Simulation Package (VASP).[40] The energy cutoff is chosen to be 1.5 times as large as the values recommended in relevant pseudopotentials. The k-point-resolved value of the Brillouin zone sampling is $0.02 \times 2\pi$ /Å. Total energy minimization is performed with a tolerance of 10^{-6} eV. The crystal structure is fully relaxed until the atomic force on each atom is less than 10^{-2} eV/Å. For the calculations with strain, atoms are relaxed with fixed lattice constants. SOC is included self-consistently throughout the calculations.

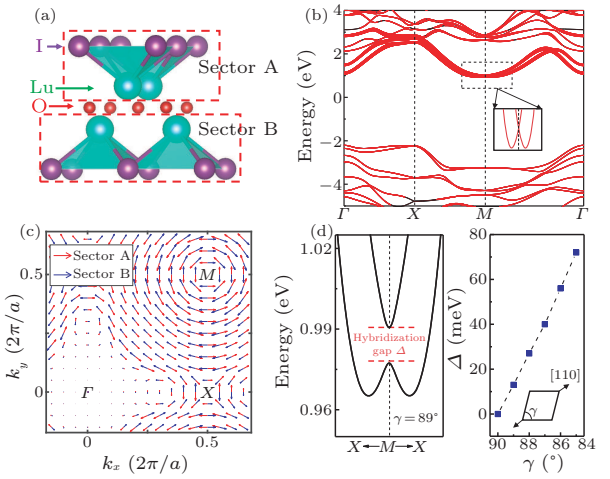

Fig. 4. (a) Crystal structure and two local sectors of LuIO. (b) Band structure (with SOC) with projection onto the Lu-d_{z^2} orbital. (c) Projected spin texture onto sectors A (red) and B (blue) for the lowest two conduction bands. (d) Hybridization gap at the M point induced by tensile strain along the [110] direction (left) and its evolution along with the monoclinic distortion γ (right).

We find that a family of rare-earth compounds LnIO (Ln = Pr, Nd, Ho, Tm, and Lu) manifests strong HSP throughout the majority of the BZ, in excellent agreement with the predictions based on our single-orbital model. As an example, LuIO crystallizes in a tetragonal nonmagnetic structure with a nonsymmorphic layer group $p4/nmm$ (No. L64), containing 6 atoms per unit cell, as shown in Fig. 4(a). The oxygen plane containing the inversion center separates the unit cell into two LuI sectors (A and B) that are connected by the inversion symmetry. The two sectors feel opposite polar fields generated by their local environments that lack inversion symmetry, indicating Rashba HSP. Figure 4(b) shows the band structure of LuIO with SOC; as discussed above, each band is at least doubly degenerate, while the nonsymmorphic symmetry guarantees the four-fold band crossing at the M point. The conduction band minimum is in the vicinity of point M, with the projected atomic orbitals dominated by the d_{z^2} character of Lu atoms, fitting with our single-orbital model very well. Therefore, we would expect the lowest two doubly degenerate conduction bands to form a pair of Rashba bands with opposite helical spin textures.

Similar to Eq. (1), the HSP is calculated by projecting the wave functions $\psi_n(\boldsymbol{k})$ with plane-wave expansion on the orbital basis (spherical harmonics) of each atomic site and summing for a given sector A or B that contains a number of sites (here is Lu and I). Again, the k-resolved hidden spin density $\boldsymbol{S}_{\mathbb{N}}^{\mathrm{A(B)}}(\boldsymbol{k})$ is calculated by summing both degenerate bands. As shown in Fig. 4(c), we find large and opposite spin polarizations of the two LuI sectors for the lowest two conduction bands. Remarkably, we observe a strong Rashba-type HSP pattern around M forming a clear domain that spans nearly 80% of the whole BZ. In addition, the spin texture around the X point is Dresselhaus-type, while around Γ, there is a small region with vanishing HSP due to the strong hopping ef-

fect between the two sectors. As discussed above, the intersector hopping term totally vanishes only along the BZ boundary X–M, and the size of large HSP domain in the whole BZ depends on the ratio between the SOC strength and hopping parameter between two sectors $\lambda_{\rm R}/t_1$, rendering ideal HSP effects in the materials with relatively strong SOC.

Discussion. We note that for the energy bands with multi-orbital features, the central physics, i.e., sector polarization and the resultant strong HSP protected by nonsymmorphic symmetry, still persists along the BZ boundary. On the other hand, the spin configuration for the other parts of the BZ could form a more complicated pattern. This is because different atomic orbitals could couple different spin textures, while the total sector-projected spin texture is the superposition of the contributions from all considered orbitals.[41] To illustrate this, we further derive a four-orbital model Hamiltonian (s, p_x, p_y, and p_z orbitals) containing 16 bands and make correspondence to the representative materials from DFT calculations. One of the main features induced by the multi-orbital nature is the retention of HSP around the Γ point for the bands with considerable p_x and p_y components, as shown in Section D of Supplementary Material. Recently, a theoretical proposal using a 1D chain model claimed that HSP vanishes in the vicinity of TRI momenta due to the coupling between sectors.[42] In contrast, our results indicate that by simply adding either nonsymmorphic symmetry or multi-orbital features,[11] an HSP system would manifest a nontrivial spin pattern for each inversion-asymmetric sector around TRI momenta. Thus, it naturally closes such debate around the practical significance of HSP, invoking further motivations to look for materials with remarkable hidden spin textures and technologically relevant properties. Since the probing beam of ARPES distinguishes different sectors by penetrating depth, the measurement of momentum-resolved HSP is highly accessible by counting the difference between the numbers of spin-up and spin-down photoelectrons. Hence, the experimental validation of our predictions on the physical effects and material candidates is strongly needed.

HSP protected by nonsymmorphic symmetry manifests two sets of spin-splitting bands that are degenerate in energy but localized at different inversion-asymmetric sectors. It would be desirable to exploit such properties for future spintronic applications, such as the modified spin field effect transistor model[5] and spin-dependent photogalvanic devices.[43] Finally, we propose that HSP might further provide a platform for tuning the hybridization between sectors to realize more exotic physics, such as topological superconductivity. In a superconductor with time-reversal symmetry and inversion symmetry, an odd-parity topological superconductor can be realized if the Fermi surface of Bloch bands encloses an odd number of TRI momenta.[25] In particular, such a kind of time-reversal-invariant topological superconductivity is proposed to exist in an interacting bilayer Rashba system,[14] of which the band model is nothing but an HSP system with a hybridization gap at the Rashba band-crossing point. The hybridization effect at the Γ point requires an appropriate buffer layer between the two Rashba layers, posing challenges to sample growing and integration.[44] In comparison, HSP systems offer us an alternative way to achieve the required band structure for experimental realization. As shown in Fig. 4(d), a tensile strain along [110] direction of LuIO breaks the screw axis symmetry and thus opens a hybridization gap Δ at the M point. The gap is 13 meV with a monoclinic distortion of the lattice $\gamma = 89°$ and increases monotonically with larger distortion. Our approach to achieve interacting Rashba bilayer bands could be used to combine with other design principles such as odd-parity pairing symmetry for the future screening of topological superconductivity.[25]

We thank Prof. Alex Zunger, Jun-Wei Luo, and Xiuwen Zhang, Dr. Wen Huang, Quansheng Wu, and Zhongjia Chen for helpful discussions.

References

[1] Winkler R 2003 *Spin-orbit Coupling Effects in Two-Dimensional Electron and Hole Systems* (Berlin, Heidelberg: Springer) Vol. 191
[2] Zhang X, Liu Q, Luo J W, Freeman A J and Zunger A 2014 *Nat. Phys.* **10** 387
[3] Liu Q, Zhang X and Zunger A 2015 *Phys. Rev. Lett.* **114** 087402
[4] Xu X, Yao W, Xiao D and Heinz T F 2014 *Nat. Phys.* **10** 343
[5] Liu Q, Guo Y and Freeman A J 2013 *Nano Lett.* **13** 5264
[6] Liu Q, Zhang X and Zunger A 2016 *Phys. Rev. B* **93** 174119
[7] Riley J M, Mazzola F, Dendzik M, Michiardi M, Takayama T, Bawden L, Granerød C, Leandersson M, Balasubramanian T and Hoesch M 2014 *Nat. Phys.* **10** 835
[8] Yao W, Wang E, Huang H, Deng K, Yan M, Zhang K, Miyamoto K, Okuda T, Li L and Wang Y 2017 *Nat. Commun.* **8** 14216
[9] Razzoli E, Jaouen T, Mottas M L, Hildebrand B, Monney G, Pisoni A, Muff S, Fanciulli M, Plumb N C and Rogalev V A 2017 *Phys. Rev. Lett.* **118** 086402
[10] Wu S L, Sumida K, Miyamoto K, Taguchi K, Yoshikawa T, Kimura A, Ueda Y, Arita M, Nagao M and Watauchi S 2017 *Nat. Commun.* **8** 1919
[11] Gotlieb K, Lin C Y, Serbyn M, Zhang W, Smallwood C L, Jozwiak C, Eisaki H, Hussain Z, Vishwanath A and Lanzara A 2018 *Science* **362** 1271
[12] Wadley P, Howells B, Andrews C *et al.* 2016 *Science* **351** 587
[13] Das T and Balatsky A V 2013 *Nat. Commun.* **4** 1972
[14] Nakosai S, Tanaka Y and Nagaosa N 2012 *Phys. Rev. Lett.* **108** 147003
[15] Ji H R and Park C H 2017 *NPG Asia Mater.* **9** e382
[16] Gautier R, Klingsporn J M, Van Duyne R P and Poeppelmeier K R 2016 *Nat. Mater.* **15** 591
[17] Suzuki R, Sakano M, Zhang Y J *et al.* 2014 *Nat. Nanotechnol.* **9** 611
[18] Cho S, Park J H, Hong J *et al.* 2018 *Phys. Rev. Lett.* **121** 186401
[19] Wang C, Lian B, Guo X, Mao J, Zhang Z, Zhang D, Gu B L, Xu Y and Duan W 2019 *Phys. Rev. Lett.* **123** 126402
[20] Falson J, Xu Y, Liao M *et al.* 2020 *Science* **367** 1454
[21] Liu Q, Zhang X, Jin H, Lam K, Im J, Freeman A J and Zunger A 2015 *Phys. Rev. B* **91** 235204
[22] Neupane M, Richardella A, Sánchez-Barriga J *et al.* 2014 *Nat. Commun.* **5** 3841
[23] Ashton M, Paul J, Sinnott S B and Hennig R G 2017 *Phys. Rev. Lett.* **118** 106101
[24] Mounet N, Gibertini M, Schwaller P *et al.* 2018 *Nat. Nan-*

otechnol. **13** 246
[25] Fu L and Berg E 2010 *Phys. Rev. Lett.* **105** 097001
[26] Qi X L, Hughes T L and Zhang S C 2010 *Phys. Rev. B* **81** 134508
[27] Dresselhaus M S, Dresselhaus G and Jorio A 2007 *Group Theory: Application to the Physics of Condensed Matter* (Berlin: Springer)
[28] Weng H, Dai X and Fang Z 2014 *Phys. Rev. X* **4** 011002
[29] Liu Q and Zunger A 2017 *Phys. Rev. X* **7** 021019
[30] Young S M, Zaheer S, Teo J C, Kane C L, Mele E J and Rappe A M 2012 *Phys. Rev. Lett.* **108** 140405
[31] Yang B J and Nagaosa N 2014 *Nat. Commun.* **5** 4898
[32] Young S M and Kane C L 2015 *Phys. Rev. Lett.* **115** 126803
[33] Bzduek T, Wu Q S, Regg A, Sigrist M and Soluyanov A A 2016 *Nature* **538** 75
[34] Liang Q F, Zhou J, Yu R, Wang Z and Weng H 2016 *Phys. Rev. B* **93** 085427
[35] Tao L L and Tsymbal E Y 2018 *Nat. Commun.* **9** 2763
[36] Santos Cottin D, Casula M, Lantz G, Klein Y, Petaccia L, Le Fèvre P, Bertran F, Papalazarou E, Marsi M and Gauzzi A 2016 *Nat. Commun.* **7** 11258
[37] Yuan L, Liu Q, Zhang X, Luo J W, Li S S and Zunger A 2019 *Nat. Commun.* **10** 906
[38] Kresse G and Joubert D 1999 *Phys. Rev. B* **59** 1758
[39] Perdew J P, Burke K and Ernzerhof M 1996 *Phys. Rev. Lett.* **77** 3865
[40] Kresse G and Furthmüller J 1996 *Comput. Mater. Sci.* **6** 15
[41] Liu Q, Zhang X, Waugh J A, Dessau D S and Zunger A 2016 *Phys. Rev. B* **94** 125207
[42] Li P and Appelbaum I 2018 *Phys. Rev. B* **97** 125434
[43] Ivchenko E L and Ganichev S D 2017 arXiv:1710.09223 [cond-mat.mes-hall]
[44] Ma H J H, Huang Z, Annadi A, Zeng S W, Wong L M, Wang S J, Venkatesan T and Ariando 2014 *Appl. Phys. Lett.* **105** 011603

Supplementary Material:

Symmetry-Assisted Protection and Compensation of Hidden Spin Polarization in Centrosymmetric Systems*

Yingjie Zhang(张英杰)[1,†], Pengfei Liu(刘鹏飞) [1,†], Hongyi Sun(孙红义) [1,†], Shixuan Zhao(赵世轩)[1], Hu Xu(徐虎)[1] and Qihang Liu(刘奇航)[1,2,3,**]

[1]*Shenzhen Institute for Quantum Science and Technology and Department of Physics, Southern University of Science and Technology, Shenzhen 518055, China*

[2]*Guangdong Provincial Key Laboratory for Computational Science and Material Design, Southern University of Science and Technology, Shenzhen 518055, China*

[3]*Center for Quantum Computing, Peng Cheng Laboratory, Shenzhen 518055, China*

*Supported by the National Natural Science Foundation of China (NSFC) under Grant No. 11874195, the Guangdong Provincial Key Laboratory of Computational Science and Material Design (Grant No. 2019B030301001) and Center for Computational Science and Engineering of Southern University of Science and Technology.

†These authors contributed equally to this work.

**Email: liuqh@sustech.edu.cn

A. SINGLE-ORBITAL TIGHT-BINDING MODEL

In this section we derive a general tight-binding model of a 2D lattice with inversion symmetry and non-symmorphic symmetry, and obtain the Hamiltonian in Eq. (1) in the main text by taking only one orbital with p4/nmm symmetry. Considering only two atoms A and B in a unit cell, as shown in Fig. S1 (a), we can construct the Bloch sum as follows,

$$\varphi_{\boldsymbol{k}n\sigma}^{A(B)}(\boldsymbol{r}) = \frac{1}{\sqrt{N}}\sum_j e^{i\boldsymbol{k}\left(\boldsymbol{R}_j+\boldsymbol{R}_{A(B)}\right)}\phi_{n\sigma}\left(\boldsymbol{r}-\boldsymbol{R}_j-\boldsymbol{R}_{A(B)}\right). \tag{A1}$$

where j labels lattice site or unit cell, $A\ and\ B$ denote the two different atoms in one unit cell and n means different atom orbital. Consequently, using the Bloch sums as the basis functions, the wavefunction of the system can be written in the following form

$$\psi_{\boldsymbol{k}n\sigma} = c_{\boldsymbol{k}n\sigma}^{A}\varphi_{\boldsymbol{k}n\sigma}^{A}(\boldsymbol{r}) + c_{\boldsymbol{k}n\sigma}^{B}\varphi_{\boldsymbol{k}n\sigma}^{B}(\boldsymbol{r}).\ (\sigma = \uparrow, \downarrow) \tag{A2}$$

We now calculate the matrix elements of Hamiltonian *H* between every pair of Bloch sums separately located at two different atoms through the conventional routine,

$$H^{AB}_{mn,\sigma\sigma'}(\boldsymbol{k}) = \left\langle \varphi^{A}_{\boldsymbol{k}m\sigma}(\boldsymbol{r}) \middle| H \middle| \varphi^{B}_{\boldsymbol{k}n\sigma'}(\boldsymbol{r}) \right\rangle$$

$$= \sum_{l} e^{i\boldsymbol{k}(\boldsymbol{R}_l - \boldsymbol{R}_j + \boldsymbol{R}_B - \boldsymbol{R}_A)} \int \phi^{*}_{n\sigma}(\boldsymbol{r} - \boldsymbol{R}_j - \boldsymbol{R}_A) H \phi_{n\sigma'}(\boldsymbol{r} - \boldsymbol{R}_l - \boldsymbol{R}_B) d\boldsymbol{r}$$

$$= \sum_l e^{i\boldsymbol{k}(\boldsymbol{R}_l - \boldsymbol{R}_j + \boldsymbol{R}_B - \boldsymbol{R}_A)} \cdot t^{AB}_{jl,mn,\sigma\sigma'} \quad .(A3)$$

As $\phi_{n\sigma}(\boldsymbol{r} - \boldsymbol{R}_j - \boldsymbol{R}_A)$ and $\phi_{n\sigma'}(\boldsymbol{r} - \boldsymbol{R}_l - \boldsymbol{R}_B)$ locate at different atoms, $H^{AB}_{mn,\sigma\sigma'}(\boldsymbol{k})$ describes the hopping between two states. Without spin degree of freedom, the hopping matrix elements in the momentum space read

$$H_{mn}(\boldsymbol{k}) = \sum_l e^{i\boldsymbol{k}(\boldsymbol{R}_l - \boldsymbol{R}_j + \boldsymbol{R}_B - \boldsymbol{R}_A)} \cdot t^{AB}_{jl,mn}, \quad \text{(A4)}$$

This Hamiltonian can be applied to both one-orbital and multi-orbital cases. The subscripts m, n can be eliminated when considering only one orbital per atom. Consequently, this is a universal expression of Hamiltonian in the frame of tight-binding method. Following the routine of Slater and Koster, the multi-orbital parameters $t^{AB}_{jl,mn}$ can be obtained from Slater-Koster parameters, as shown in Table SI. For example, the nearest neighbor hopping between p_x and p_y orbitals can be expressed by $lm(V_{pp\sigma} - V_{pp\pi})$, where *l, m*, and *n* are direction cosines of the vector from one atom to the nearest atom.

Table SI: The hopping parameters between *s* and *p* orbitals $t_{m,n}$ can be combined by Slater-Koster parameters using the direction cosine *l, m*, and *n* of the vector from the left atom to the right atom. Other matrix elements can be found by permuting indices [1].

$t_{s,s}$	$V_{ss\sigma}$	$t_{x,x}$	$l^2V_{pp\sigma} + (1 - l^2)V_{pp\pi}$
$t_{s,x}$	$lV_{sp\sigma}$	$t_{x,y}$	$lm(V_{pp\sigma} - V_{pp\pi})$
$t_{x,s}$	$-lV_{sp\sigma}$	$t_{y,z}$	$mn(V_{pp\sigma} - V_{pp\pi})$

Now we can carry out the process in a concrete crystal structure. In a crystal with displacement d_z between A and B sublattices along the z direction as shown in Fig. S1(a), one atom A have four nearest (next nearest) neighbor atoms B (A) and the relative position vectors between one atom A and its neighbors thus become $\boldsymbol{d}_{11}, \boldsymbol{d}_{12}, \boldsymbol{d}_{13}, \boldsymbol{d}_{14}$ $(\boldsymbol{d}_{21}, \boldsymbol{d}_{22}, \boldsymbol{d}_{23}, \boldsymbol{d}_{24})$. The corresponding hopping parameters are $t_{11}, t_{12}, t_{13}, t_{14}$ $(t_{21}, t_{22}, t_{23}, t_{24})$ respectively, as shown in Fig. S1(a), some of which are equal according to the symmetry of crystal. Therefore, Eq. (A4) with only one atom orbital can be rewritten as

$$H_{jl}(\boldsymbol{k}) = \sum_l e^{i\boldsymbol{k}\boldsymbol{d}_{jl}} \cdot t_{jl}. \tag{A5}$$

Especially, for the p4/nmm structure (D_{4h}) in Fig. 1(a) in the main text, we can further simplify the Hamiltonian and obtain the first two terms of Eq. (1) in the main text as (taking $1/a$ as the unit of k)

$$H_0 = t_1 \cos\frac{k_x}{2}\cos\frac{k_y}{2}\tau_x + t_2\left(\cos k_x + \cos k_y\right)\tau_0, \tag{A6}$$

where $\boldsymbol{\tau}$ is the Pauli matrix depicting the freedom of A and B sublattices.

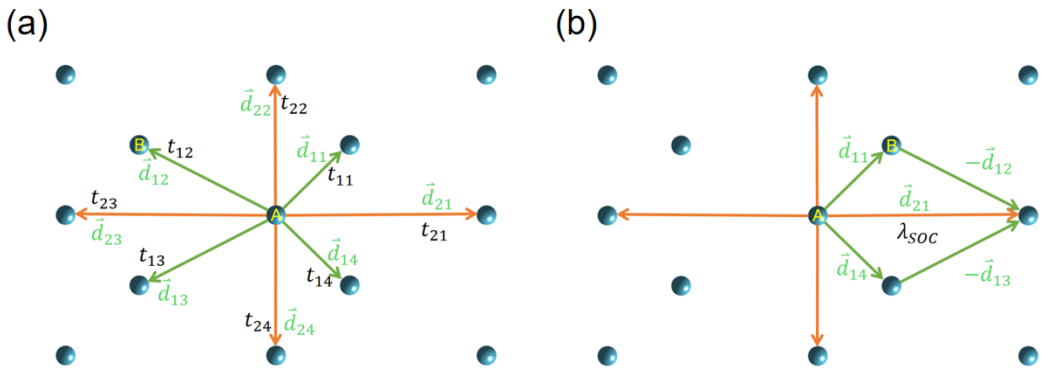

Fig. S1: (a) Position vectors from an atom A to its nearest (next nearest) neighbor atoms B(A) are labeled by $\boldsymbol{d}_{11}, \boldsymbol{d}_{12}, \boldsymbol{d}_{13}, \boldsymbol{d}_{14}$ $(\boldsymbol{d}_{21}, \boldsymbol{d}_{22}, \boldsymbol{d}_{23}, \boldsymbol{d}_{24})$ with green color and the corresponding hopping parameters are labeled by $t_{11}, t_{12}, t_{13}, t_{14}(t_{21}, t_{22}, t_{23}, t_{24})$ with black color. (b) $\boldsymbol{d}_{1j}$ and $\boldsymbol{d}_{1l}$ are the two nearest bonds connecting the next-nearest neighbors $\boldsymbol{d}_{2j}$, along which the spin-orbital coupling occurs.

We next consider the SOC term of the Hamiltonian in the multi-orbital case as

follows,

$$H_{soc} = \xi_0 \left(\frac{L_+ s_- + L_- s_+}{2} + L_z s_z \right), \tag{A7}$$

where $s_\pm = s_x \pm i s_y$ and $L_\pm = L_x \pm i L_y$. Only the SOC between the same sublattice is taken into account. The concrete SOC term can be obtained by calculating the mean value of Eq. (A7). For example, the SOC term between $|pz\uparrow\rangle$ and $|px\downarrow\rangle$ reads $\langle pz\uparrow|H_{soc}|px\downarrow\rangle = \xi_0$. A straightforward calculation leads to the on-site SOC in the representation $\{s, p_x, p_y, p_z\}\otimes\{\uparrow,\downarrow\}$:

$$H_{soc} = \frac{\xi_0}{2} h_{so}, \tag{A8}$$

where all elements in h_{so} can be found in Table SII. As we can see in the table, the SOC effect of one orbital is totally induced by another orbital and it is difficult to get SOC term just from a single orbital.

Table SII: The values of SOC among atomic orbitals that are used in h_{so}. The nonzero SOC terms only exist between orbits of the same site. $\sigma_{x,y,z}$ are Pauli matrices acting on the spin space.

	s	p_x	p_y	p_z
s	0	0	0	0
p_x	0	0	$-i\sigma_z$	$i\sigma_y$
p_y	0	$i\sigma_z$	0	$-i\sigma_x$
p_z	0	$-i\sigma_y$	$i\sigma_x$	0

However, we can also construct the single-orbital SOC Hamiltonian by symmetry consideration of the lattice. In the structure with C_{2h} symmetry in Fig. 3(c) of main text, an electron hopping from an atom A to its next nearest neighbor atom A can feel an effective field coming from local asymmetry. Considering symmetry of the structure, the original SOC term $-\frac{\hbar}{4m_0^2c^2}(\boldsymbol{F}\times\boldsymbol{p})\cdot\boldsymbol{\sigma}$ can be replaced by $-i\eta_R(\boldsymbol{d}_{1j}\times\boldsymbol{d}_{1l})\cdot\boldsymbol{\sigma}$, where η_R is a parameter and $\boldsymbol{d}_{1j}$ and $\boldsymbol{d}_{1l}$ are vectors along the two nearest bonds connecting the next nearest neighbors $\boldsymbol{d}_{2j}$, as shown in Fig. S1(b). For a lattice

structure with C_{2h} symmetry, to get the SOC term in k space, we should sum over the four next nearest neighbor SOC effects and the term $\boldsymbol{d}_{1j} \times \boldsymbol{d}_{1l}$ in k space then becomes

$$[\boldsymbol{d}_{14} \times (-\boldsymbol{d}_{13}) + \boldsymbol{d}_{11} \times (-\boldsymbol{d}_{12})]e^{i\boldsymbol{k}\boldsymbol{d}_{21}} + [\boldsymbol{d}_{12} \times (-\boldsymbol{d}_{11}) + \boldsymbol{d}_{13} \times (-\boldsymbol{d}_{14})]e^{i\boldsymbol{k}\boldsymbol{d}_{23}}$$
$$+ [\boldsymbol{d}_{11} \times (-\boldsymbol{d}_{14}) + \boldsymbol{d}_{12} \times (-\boldsymbol{d}_{13})]e^{i\boldsymbol{k}\boldsymbol{d}_{22}} + [\boldsymbol{d}_{13} \times (-\boldsymbol{d}_{12}) + \boldsymbol{d}_{14} \times (-\boldsymbol{d}_{11})]e^{i\boldsymbol{k}\boldsymbol{d}_{24}}$$
$$= [\boldsymbol{d}_{14} \times (-\boldsymbol{d}_{13}) + \boldsymbol{d}_{11} \times (-\boldsymbol{d}_{12})]\left(e^{i\boldsymbol{k}\boldsymbol{d}_{21}} - e^{i\boldsymbol{k}\boldsymbol{d}_{23}}\right) + [\boldsymbol{d}_{11} \times (-\boldsymbol{d}_{14}) + \boldsymbol{d}_{12} \times (-\boldsymbol{d}_{13})](e^{i\boldsymbol{k}\boldsymbol{d}_{22}} - e^{i\boldsymbol{k}\boldsymbol{d}_{24}})$$
$$= [\boldsymbol{d}_{14} \times (-\boldsymbol{d}_{13}) + \boldsymbol{d}_{11} \times (-\boldsymbol{d}_{12})](2i\sin k_x a) + [\boldsymbol{d}_{11} \times (-\boldsymbol{d}_{14}) + \boldsymbol{d}_{12} \times (-\boldsymbol{d}_{13})](2i\sin k_y b). \quad \text{(A9)}$$

As for the p4/nmm (D_{4h}) structure, the SOC term can be written as

$$H_{soc} = \lambda_R\left(\sigma_y sin k_x - \sigma_x sin k_y\right)\tau_z. \quad \text{(A10)}$$

Together with Eq. (A6), we obtain the single-orbital Hamiltonian $H(\boldsymbol{k}) = H_0 \otimes \sigma_0 + H_{soc}$ (σ_0 is 2×2 identity matrix), which is just Eq. (1) in the main text.

B. ANALYTICAL SOLUTION OF THE SINGLE-ORBITAL MODEL

As mentioned above, we have obtained Eq. (1) in the main text together with Eq. (A6) and Eq. (10), in which we have selected the basis to be ($|\mathrm{A}\uparrow\rangle, |\mathrm{A}\downarrow\rangle, |\mathrm{B}\uparrow\rangle, |\mathrm{B}\downarrow\rangle$). By defining $M = t_1 \cos(k_x/2)\cos(k_y/2)$, $N = t_2(\cos k_x + \cos k_y)$, $D_+ = \lambda(\sin k_y + i \sin k_x)$, $D_- = D_+^\dagger$, $F = \sqrt{M^2 + D_+ D_-}$, we can rewrite the Hamiltonian in the form of simplified matrix:

$$H = \begin{bmatrix} N & -D_+ & M & 0 \\ -D_- & N & 0 & M \\ M & 0 & N & D_+ \\ 0 & M & D_- & N \end{bmatrix}. \quad \text{(A11)}$$

The operators of three physical properties $\hat{P}^{sec}$, $\widehat{\boldsymbol{S}}^A$ and $\widehat{\boldsymbol{S}}^B$ can be written in matrix form

$$\begin{aligned} \widehat{\boldsymbol{S}}^A &= |A\rangle\langle A|\boldsymbol{\sigma} = \tau_A \boldsymbol{\sigma}, \\ \widehat{\boldsymbol{S}}^B &= |B\rangle\langle B|\boldsymbol{\sigma} = \tau_B \boldsymbol{\sigma}, \\ \hat{P}^{sec} &= |A\rangle\langle A| - |B\rangle\langle B| = \tau_z, \end{aligned} \quad \text{(A12)}$$

where τ_z and $\boldsymbol{\sigma}$ are the Pauli matrices on orbital and spin degrees of freedom and τ_A and τ_B are projection operators on A and B sectors

$$\tau_A = \begin{pmatrix} 1 & 0 \\ 0 & 0 \end{pmatrix}, \tau_B = \begin{pmatrix} 0 & 0 \\ 0 & 1 \end{pmatrix}. \quad \text{(A13)}$$

From the above we can find the relation between sector polarization and projected spin

polarization, $\widehat{\boldsymbol{S}}^A - \widehat{\boldsymbol{S}}^B = \hat{P}^{sec}\boldsymbol{\sigma}$. To demonstrate these physical properties, we should solve the Hamiltonian in Eq. (A11) first. By solving it analytically, we can get the eigen energies to be $E_{1,2} = N - F$ and $E_{3,4} = N + F$ with four orthogonal eigen functions:

$$\phi_1 = \frac{1}{\sqrt{2}}\begin{pmatrix} 1 \\ D_-/F \\ -M/F \\ 0 \end{pmatrix}, \phi_2 = \frac{1}{\sqrt{2}}\begin{pmatrix} 0 \\ -M/F \\ -D_+/F \\ 1 \end{pmatrix}, \phi_3 = \frac{1}{\sqrt{2}}\begin{pmatrix} 1 \\ -D_-/F \\ M/F \\ 0 \end{pmatrix}, \phi_4 = \frac{1}{\sqrt{2}}\begin{pmatrix} 0 \\ M/F \\ D_+/F \\ 1 \end{pmatrix}. \quad \text{(A14)}$$

All of the energies and eigen functions are functions of wavevector $\boldsymbol{k}$, from which we can readily get analytical expressions of other physical quantities. The results of sector polarization and HSP can be found in the main text, in which the origin of strong HSP at the BZ is also demonstrated.

Actually, the solution in Eq. (A14) is just a particular solution. More generally, by applying linear combinations of ϕ_1, ϕ_2 (ϕ_3, ϕ_4) we can form different sets of basis of the degenerate subspace with eigen energy $E_{1,2}$ ($E_{3,4}$). Then, it seems that there is a gauge problem here. To check whether HSP is gauge invariant, we can casually construct a set of new doubly degenerate states $\phi'_1 = c_1\phi_1 + c_2\phi_2$ and $\phi'_2 = c_3\phi_1 + c_4\phi_2$. We then investigate whether the HSP remains unchanged after this transformation. Then, to ensure the basis transforming matrix to be unitary we should require $c_4^* / c_3^* = -c_1 / c_2$ and the new degenerate states become $\phi'_1 = c_1\phi_1 + c_2\phi_2$ and $\phi'_2 = c_2^*\phi_1 - c_1^*\phi_2$, where $|c_1|^2 + |c_2|^2 = 1$. Using ϕ'_1 and ϕ'_2, we get the physical properties at different coefficients c_1, which is shown in Fig. S2.

$$P_1^{sec} = \frac{1}{2}(|c_1|^2 - |c_2|^2) + \frac{1}{2F^2}[(|c_2|^2 - |c_1|^2)(M^2 - D^2) - 2M(c_1^*c_2D_+ + c_1c_2^*D_-)]$$

$$P_2^{sec} = \frac{1}{2}(|c_2|^2 - |c_1|^2) + \frac{1}{2F^2}[-(|c_2|^2 - |c_1|^2)(M^2 - D^2) + 2M(c_1^*c_2D_+ + c_1c_2^*D_-)]$$

$$s_{1x}^A = \frac{1}{2}[|c_1|^2(D_+ + D_-) - M(c_1c_2^* + c_1^*c_2)]/F \quad \text{(A15)}$$

$$s_{2x}^A = \frac{1}{2}[|c_2|^2(D_+ + D_-) + M(c_1c_2^* + c_1^*c_2)]/F$$

$$s_{1y}^A = \frac{i}{2}[|c_1|^2(D_+ - D_-) - M(c_1c_2^* - c_1^*c_2)]/F$$

$$s_{2y}^A = \frac{i}{2}[|c_2|^2(D_+ - D_-) + M(c_1c_2^* - c_1^*c_2)]/F.$$

Both of P_n^{sec} and s_n^A for a single energy state vary with the coefficient c_1, where the subscript n means on the state of ϕ'_n. The gauge dependence is because one cannot

measure a physical property of just one single state in a degenerate system. Adding the effect of E_1 and E_2, the expectation values of the components of HSP are $s^A_{(1+2)x} = s^A_{1x} + s^A_{2x} = \frac{1}{2}[(D_+ + D_-)]/F$, $s^A_{(1+2)y} = s^A_{1y} + s^A_{2y} = \frac{i}{2}[(D_+ - D_-)]/F$, which obviously have no relation with the coefficient c_1. The result is shown in Fig. S2(e) and we only figure one green line as the property does not change depending on the coefficient c_1. This indicate that HSP is indeed a physical property that is gauge independent. The value in the Fig. S2(e) is nonzero and stable, which can benefit its measurement by spin-ARPES. We also find that the value reaches its maximum at the BZ boundary X-M as the hopping effect between A and B disappears, indicating strong HSP protected by nonsymmorphic symmetry.

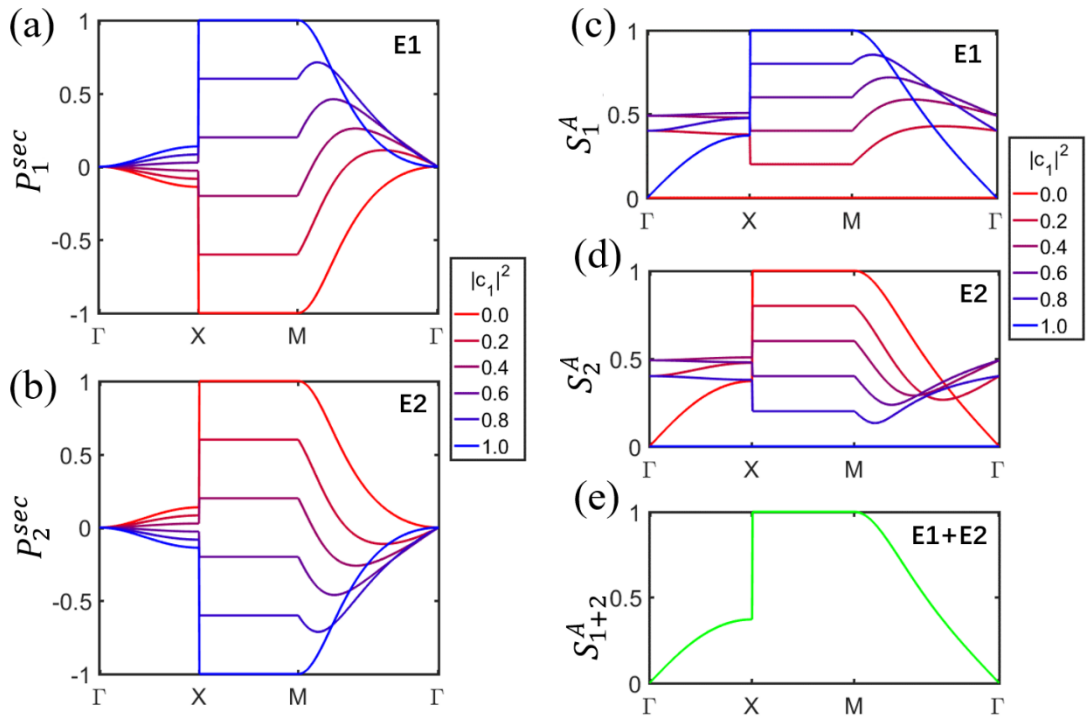

Fig. S2: (a) and (b) are sector polarizations P_n^{sec} of E_1 and E_2 on different coefficients c_1. The sector polarizations of the two states are in opposite value, which means the total effect of them is zero. This is because sector A and sector B are in equal status in a centrosymmetric system and the expectation value should be zero. (c) and (d) are the sector projected spin polarizations $S^A_{\mathbb{m}}$ on sector A for E_1 and E_2 at

different coefficients c_1. The same with P_n^{sec}, the values of $S_{\mathbb{m}}^A$ also vary with c_1. (e) The expectation values of $S_{\mathbb{m}}^A$ for both E_1 and E_2 at different c_1. The values are all the same and we only figure one line of them, indicating that HSP does not vary with basis transformation.

C. CORRESPONDENCE BETWEEN LAYER GROUPS AND 3D SPACE GROUPS

Layer groups are 3D groups with 2D translation symmetry, but we can still use 3D crystal systems and point groups to classify layer groups [2]. All layer groups, by definition, have no translation symmetry along basis vector *c* which prohibits certain symmetry operations, for instance, screw rotation along the *c* axis, more than 2-fold rotation with the axis perpendicular to *c*, etc. Therefore, cubic crystal system does not exist for layer groups.

For each layer group and a randomly chosen position within the empty lattice, layer group generators provided by the Bilbao Crystallographic Server [3] produce a set of equivalent positions, forming a set of general positions (SGP). We thus construct a "pseudo crystal structure" by filling this SGP by atoms into the empty lattice. Then, we can get another SGP by choosing another random position and following the same way. After the pseudo crystal structure is constructed by inputting several SGP, we can easily obtain the corresponding 3D space group from the existing modules such as ASE [4] and Spglib [5].

We have tried to put *n* (*n* = 1, 2, …6) SGP in the empty lattice for each layer groups. We found that space groups corresponding to a particular layer group converge with *n* > 2, for which the correspondence between space group and layer group is given (see also Table SIII). We note that two layer groups may correspond to the same space group for monoclinic and orthorhombic layer groups which is due to the inequivalence of *c* axis and the other two axis, including (L3, L8), (L4, L11), (L5, L12), (L6, L14), (L7, L16), (L23, L27), (L24, L31), (L28, L29) and (L40, L41). Such situation does not appear for tetragonal, trigonal and hexagonal layer groups since 4-fold, 3-fold, and 6-fold rotation axes or rotation-reflection axes must be along the *c* axis. Finally, we note that our results

for $n > 2$ are mostly consistent with those of Ref. [6], which used a different method called geometric algebra to construct the correspondence, except for layer group L35 which correspond to space group 38.

Table SIII. Correspondence between layer groups and space groups with different sets of general positions (SGP). The underlined space groups are different from the space groups determined by more than 2 SGP.

		Space group		
Crystal system	Layer group	> 2 SGP	2 SGP	1 SGP
Triclinic	L1 p1	1 P1	<u>2 $P\bar{1}$</u>	<u>10 P2/m</u>
	L2 $p\bar{1}$	2 $P\bar{1}$	2 $P\bar{1}$	2 $P\bar{1}$
Monoclinic	L3 p112	3 P2	3 P2	<u>10 P2/m</u>
	L4 p11m	6 Pm	6 Pm	<u>10 P2/m</u>
	L5 p11a	7 Pc	7 Pc	<u>13 P2/c</u>
	L6 p112/m	10 P2/m	10 P2/m	10 P2/m
	L7 p112/a	13 P2/c	13 P2/c	13 P2/c
	L8 p211	3 P2	3 P2	<u>10 P2/m</u>
	L9 $p2_111$	4 $P2_1$	4 $P2_1$	<u>11 $P2_1$/m</u>
	L10 c211	5 C2	5 C2	<u>12 C2/m</u>
	L11 pm11	6 Pm	6 Pm	<u>47 Pmmm</u>
	L12 pb11	7 Pc	7 Pc	<u>51 Pmma</u>
	L13 cm11	8 Cm	8 Cm	<u>65 Cmmm</u>
	L14 p2/m11	10 P2/m	10 P2/m	10 P2/m
	L15 $p2_1/m11$	11 $P2_1/m$	11 $P2_1/m$	11 $P2_1/m$
	L16 p2/b11	13 P2/c	13 P2/c	13 P2/c
	L17 $p2_1/b11$	14 $P2_1/c$	14 $P2_1/c$	14 $P2_1/c$
	L18 c2/m11	12 C2/m	12 C2/m	12 C2/m
Orthorhombic	L19 p222	16 P222	16 P222	16 P222
	L20 $p2_122$	17 $P222_1$	17 $P222_1$	17 $P222_1$

	L21 $p2_12_12$	18 $P2_12_12$	18 $P2_12_12$	18 $P2_12_12$
	L22 c222	21 C222	21 C222	21 C222
	L23 pmm2	25 Pmm2	25 Pmm2	47 Pmmm
	L24 pma2	28 Pma2	28 Pma2	51 Pmma
	L25 pba2	32 Pba2	32 Pba2	55 Pbam
	L26 cmm2	35 Cmm2	35 Cmm2	65 Cmmm
	L27 pm2m	25 Pmm2	25 Pmm2	47 Pmmm
	L28 $pm2_1b$	26 $Pmc2_1$	26 $Pmc2_1$	51 Pmma
	L29 $pb2_1m$	26 $Pmc2_1$	26 $Pmc2_1$	51 Pmma
	L30 pb2b	27 Pcc2	27 Pcc2	49 Pccm
	L31 pm2a	28 Pma2	28 Pma2	51 Pmma
	L32 $pm2_1n$	31 $Pmn2_1$	31 $Pmn2_1$	59 Pmmn
	L33 $pb2_1a$	29 $Pca2_1$	29 $Pca2_1$	57 Pbcm
	L34 pb2n	30 Pnc2	30 Pnc2	53 Pmna
	L35 cm2m	38 Amm2	38 Amm2	65 Cmmm
	L36 cm2e	39 Aem2	39 Aem2	67 Cmme
	L37 pmmm	47 Pmmm	47 Pmmm	47 Pmmm
	L38 pmaa	49 Pccm	49 Pccm	49 Pccm
	L39 pban	50 Pban	50 Pban	50 Pban
	L40 pmam	51 Pmma	51 Pmma	51 Pmma
	L41 pmma	51 Pmma	51 Pmma	51 Pmma
	L42 pman	53 Pmna	53 Pmna	53 Pmna
	L43 pbaa	54 Pcca	54 Pcca	54 Pcca
	L44 pbam	55 Pbam	55 Pbam	55 Pbam
	L45 pbma	57 Pbcm	57 Pbcm	57 Pbcm
	L46 pmmn	59 Pmmn	59 Pmmn	59 Pmmn
	L47 cmmm	65 Cmmm	65 Cmmm	65 Cmmm
	L48 cmme	67 Cmme	67 Cmme	67 Cmme
Tetragonal	L49 p4	75 P4	75 P4	83 P4/m

	L50 p$\bar{4}$	81 P$\bar{4}$	81 P$\bar{4}$	81 P$\bar{4}$
	L51 p4/m	83 P4/m	83 P4/m	83 P4/m
	L52 p4/n	85 P4/n	85 P4/n	85 P4/n
	L53 p422	89 P422	89 P422	89 P422
	L54 p42$_1$2	90 P42$_1$2	90 P42$_1$2	90 P42$_1$2
	L55 p4mm	99 P4mm	99 P4mm	123 P4/mmm
	L56 p4bm	100 P4bm	100 P4bm	127 P4/mbm
	L57 p$\bar{4}$2m	111 P$\bar{4}$2m	111 P$\bar{4}$2m	111 P$\bar{4}$2m
	L58 p$\bar{4}$2$_1$m	113 P$\bar{4}$2$_1$m	113 P$\bar{4}$2$_1$m	113 P$\bar{4}$2$_1$m
	L59 p$\bar{4}$m2	115 P$\bar{4}$m2	115 P$\bar{4}$m2	115 P$\bar{4}$m2
	L60 p$\bar{4}$b2	117 P$\bar{4}$b2	117 P$\bar{4}$b2	117 P$\bar{4}$b2
	L61 p4/mmm	123 P4/mmm	123 P4/mmm	123 P4/mmm
	L62 p4/nbm	125 P4/nbm	125 P4/nbm	125 P4/nbm
	L63 p4/mbm	127 P4/mbm	127 P4/mbm	127 P4/mbm
	L64 p4/nmm	129 P4/nmm	129 P4/nmm	129 P4/nmm
Trigonal	L65 p3	143 P3	143 P3	187 P$\bar{6}$m2
	L66 p$\bar{3}$	147 P$\bar{3}$	147 P$\bar{3}$	164 P$\bar{3}$m1
	L67 p312	149 P312	149 P312	187 P$\bar{6}$m2
	L68 p321	150 P321	150 P321	164 P$\bar{3}$m1
	L69 p3m1	156 P3m1	156 P3m1	187 P$\bar{6}$m2
	L70 p31m	157 P31m	157 P31m	191 P6/mmm
	L71 p$\bar{3}$1m	162 P$\bar{3}$1m	162 P$\bar{3}$1m	191 P6/mmm
	L72 p$\bar{3}$m1	164 P$\bar{3}$m1	164 P$\bar{3}$m1	164 P$\bar{3}$m1
Hexagonal	L73 p6	168 P6	168 P6	191 P6/mmm
	L74 p$\bar{6}$	174 P$\bar{6}$	174 P$\bar{6}$	187 P$\bar{6}$m2
	L75 p6/m	175 P6/m	175 P6/m	191 P6/mmm
	L76 p622	177 P622	177 P622	191 P6/mmm
	L77 p6mm	183 P6mm	183 P6mm	191 P6/mmm
	L78 p$\bar{6}$m2	187 P$\bar{6}$m2	187 P$\bar{6}$m2	187 P$\bar{6}$m2

L79 p$\bar{6}$2m	189 P$\bar{6}$2m	189 P$\bar{6}$2m	191 P6/mmm
L80 p6/mmm	191 P6/mmm	191 P6/mmm	191 P6/mmm

D. MULTI-ORBITAL TIGHT-BINDING MODEL AND MATERIAL REALIZATION

Following the same approach of getting Eq. (1) in the main text, we can obtain the multi-orbital Hamiltonian of the p4/nmm system from Eq. (A4) and Eq. (A8), where nonsymmorphic symmetry can be guaranteed by a displacement in the z direction from the structure parameters $\boldsymbol{d}_{jl}$. The hopping parameters $t_{m,n}$ can be combined by Slater-Koster parameters as shown in Table SI at Section A, where the four parameters $V_{ss\sigma}$, $V_{sp\sigma}$, $V_{pp\sigma}$, and $V_{pp\pi}$ correspond to the σ and π bonds formed by s and p orbitals.

Most of the hidden spin properties discussed during the discussion of single-orbital Hamiltonian, such as strong HSP protected by nonsymmorphic symmetry, are also found here. That shows the consistency between our single-orbital model and multi-orbital model. The phenomenon of HSP also exists over the whole Brillouin zone despite that the amplitudes for various bands change with the momentum in different manners. This is because the dominant orbital component of one band can vary with $\boldsymbol{k}$. HSP of s or p_z dominated band is immune to hopping effect at the Brillouin zone boundary protected by nonsymmorphic symmetry while suffers significant suppression near the Γ point, as shown in Fig. S4(a), which is in agreement with results obtained in single-orbital model. With a displacement of sector A along the x direction, the symmetry of D_{4h} structure is reduced to C_{2h} by breaking the screwing axis along the x direction, resulting in a smaller HSP strength along X-M in the Brillouin zone as shown in Fig. S4(b). On the other hand, HSP of a p_x/p_y dominant band forms a Rashba-type helical spin texture with a large value around the Γ point, as shown in Fig. S4(c). To illustrate this in material base, we also perform the first-principle calculation on a representative multi-orbital material $Bi_2Cl_2O_2$ with p4/nmm symmetry. As shown in Fig. S4(d), we find significant Rashba-type HSP around the Γ point for the second highest,

px/py dominated valance band of $Bi_2Cl_2O_2$, which is good agreement with our multi-orbital tight-binding model.

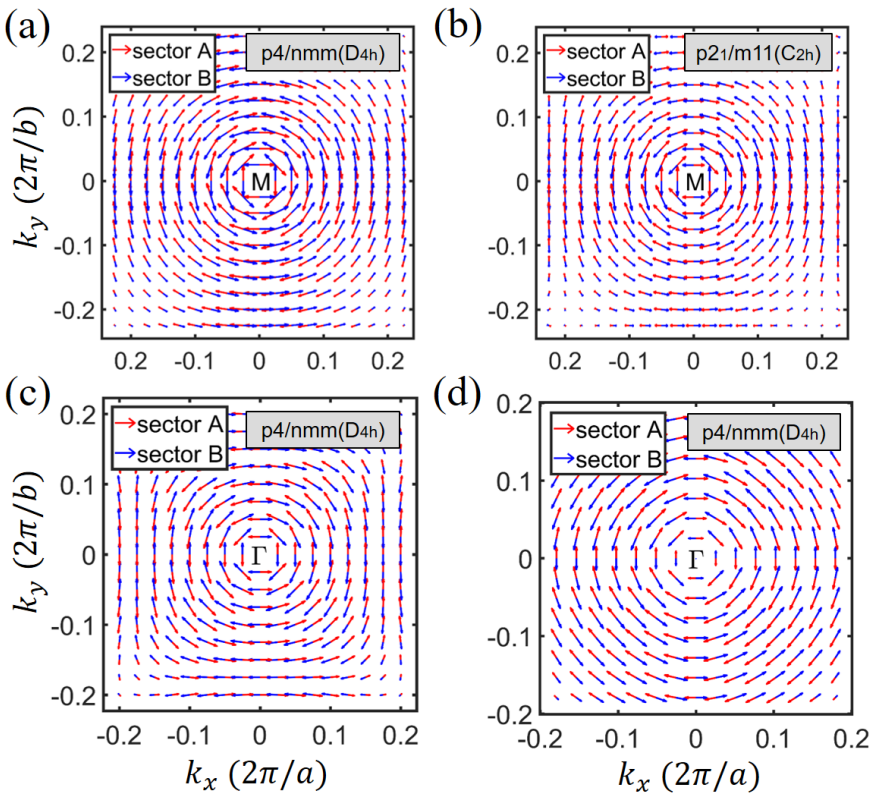

Fig. S4: Projected spin texture onto sector A (red) and B (blue) around the M point for a *s/pz* dominanted band from the multi-orbital model with (a) D_{4h} and (b) C_{2h} symmetry. Projected spin texture around the Γ point for a *px/py* dominanted band from (c) the multi-orbital model, and (d) first-principle calculation on monolayer $Bi_2Cl_2O_2$.

References

[1] C.-C. Liu, H. Jiang, and Y. Yao, Phys. Rev. B **84**, 195430 (2011).

[2] V. c. Kopsky and D. B. Litvin, (2010).

[3] M. I. Aroyo, J. M. Perez-Mato, C. Capillas, E. Kroumova, S. Ivantchev, G. Madariaga, A. Kirov, and H. Wondratschek, Zeitschrift für Kristallographie - Crystalline Materials **221**, 15 (2006).

[4] A. H. Larsen, J. J. Mortensen, J. Blomqvist, I. E. Castelli, R. Christensen, M. Dułak, J. Friis, M. N. Groves, B. Hammer, and C. Hargus, J. Phys.: Condens. Matter **29**, 273002 (2017).

[5] A. Togo and I. Tanaka, (2018).

[6] E. Hitzer and D. Ichikawa, Advances in Applied Clifford Algebras **23**, 887 (2013).